# Observational Study of a Multiple Microburst-Producing Storm Part III: Vorticity Budgets

YEONG-JER LIN[1] AND P. G. LAPOINTE[2]

*(Received 13 March 1991; Revised 29 July 1991)*

## ABSTRACT

A vorticity component and budget analysis in three dimension is conducted for the subcloud layer of two microburst-producing storms using dual-Doppler derived winds. This study examines the vorticity associated with a single microburst-producing storm which occurred on 14 July 1982 and a multiple microburst-producing storm which occurred on 5 August 1982 in Colorado.

Results show that horizontal vorticity centers are coincident with strong horizontal gradients of vertical velocity and with areas of strong vertical shear. These gradients are maximized along the edges of downrushing air and along gust fronts. Regions of high speed low-level winds have a core horizontal vorticity above them.

A vorticity budget analysis of the advection, divergence and tilting terms, comprising the vorticity component equations, shows the magnitude of these terms to be greater in the microburst domain than in the storm domain. This indicates that the strongest forcing and advection takes place within small regions of the storms. The diverging outflow of the microburst in both cases weakens any existing positive vorticity in the microburst region ($z < 1$ *km*).

The differences in storm structure allow examination of the vorticity of a simple, nearly circular-symmetric microburst and that of a microburst within a complicated flow field. This leads to different voricity distributions and budgets.

## 1. INTRODUCTION

In Part I of this study, Lin *et al.* (1991) investigated the structure and internal dynamics of a multiple microburst-producing storm in Colorado using dual-Doppler data collected at 1845, 1847 and 1850 MDT (mountain daylight time) on 5 August 1982. The results were then compared to those for the simple case (14 July 1982) in Part II of this study (Lin and Coover, 1991). Findings

[1] *Department of Earth and Atmospheric Sciences, Saint Louis University, U. S. A.*

[2] *Air Weather Service, U. S. Air Force*

revealed that both misocyclone and horizontal vortex (rotor) play an important role in affecting the structure of a microburst-producing storm.

In the other case study of a microburst-producing storm, Kessinger *et al.* (1988) investigated the subcloud layer of a multicellular storm in Colorado using multiple Doppler derived winds. Their storm produced misocyclones, which are horizontal cyclonic circulation centers with diameters of $2 \sim 4$ *km* (Fujita, 1985), downbursts, and horizontal vortex circulations. Kessinger *et al.* (1988) found that the misocyclone characteristics differ from those of mesocyclone by having a vorticity maximum near cloud base instead of at low-levels and that the low-level positive vertical vorticity is weakened by the low-level divergence associated with the microburst. They also pointed out that rotors form along the edge of these misocyclones and storm downdrafts, and propagate away from the storm. These rotors have also been associated with regions of maximum surface winds.

The importance of the rotor in causing damage as well as being an aviation hazard has recently come under more study. The rotor core from the microburst outflows is associated with lower pressure than its surroundings, which acts to accelerate the surface winds (Waranauskas, 1985). The author suggested that the axis of the rotor and the microburst coincide, thereby linking the rotor as a cause or enhancement of the microburst. Linden and Simpson (1985) stated that the wind shear and downward motion associated with the back of the rotor may be responsible for the danger of flying through a microburst. An additional mechanism for intensifying the leading-edge vortex may be the existence of rotation in the descending air.

The purpose of this study in Part III is to investigate three-dimensional vorticities associated with microbursts. Vorticity budgets for the subcloud layer of two microburst-producing storms described previously in Part I and II will be examined using Doppler derived wind fields. A comparison will be made as to the mechanisms responsible for one storm's vorticity field to that for another storm. The ultimate goal is to better understand the importance of the microburst and its associated structure to the generation of vorticity.

## 2. DATA AND ANALYSIS PROCEDURES

The data and analysis procedures for the complex case (5 August 1982) have been detailed in Part I of this study. There were five analysis levels in the vertical ranging from 0.25 to 1.25 *km* with a horizontal grid spacing of 0.5 *km*. Dual-Doppler data at 1845, 1847 and 1850 MDT were objectively analyzed using the horizontal domain of 15 *km* by 15 *km*. Only those data with a high signal-to-noise ratio were accepted for analysis.

In the same manner, dual-Doppler data for the simple case (14 July 1982)

at 1647 and 1649 MDT were carefully analyzed over the horizontal domain of 10 km by 10 *km* using a 0.5 *km* horizontal grid spacing. The vertical grid spacing varied from 0.25 *km* for the levels below 1 *km* to 0.5 *km* for those above 1 *km*. For details, see studies by Lin and Hughes (1987) and Lin and Coover (1991).

We employed two radial velocity equations, the anelastic continuity equation, and an empirical formula of terminal fall speed to obtain the horizontal wind components. The vertical velocity component was computed from the anelastic continuity equation by integrating upward from the surface. Subsequently, fields of deviation perturbation pressure and temperature were retrieved from the three momentum equations using the Doppler derived winds.

## 3. METHODOLOGY

The vertical vorticity equation is obtained by taking curl of the equation of motion in vector form. Upon recognizing the small effect the earth's rotation has on the absolute vorticity, one obtains an expression for the relative vorticity along the vertical axis:

$$\frac{\partial \zeta}{\partial t} = \underset{A}{-\vec{v}_h \cdot \vec{\nabla}_h \zeta} \underset{B}{- w \frac{\partial \zeta}{\partial z}} \underset{C}{- \zeta \left( \vec{\nabla}_h \cdot \vec{v}_h + \frac{\partial w}{\partial z} \right)} + \underset{D}{\left( \xi \frac{\partial w}{\partial x} + \eta \frac{\partial w}{\partial y} + \zeta \frac{\partial w}{\partial z} \right)} - \underset{E}{\left( \frac{\partial \alpha}{\partial x} \frac{\partial p}{\partial y} - \frac{\partial \alpha}{\partial y} \frac{\partial p}{\partial x} \right)} + \underset{F}{\left( \frac{\partial fy}{\partial x} - \frac{\partial fx}{\partial y} \right)} \tag{1}$$

where

$\xi = \dfrac{\partial w}{\partial y} - \dfrac{\partial v}{\partial z}$, the x-component relative vorticity;

$\eta = \dfrac{\partial u}{\partial z} - \dfrac{\partial w}{\partial x}$, the y-component relative vorticity;

and

$\zeta = \dfrac{\partial v}{\partial x} - \dfrac{\partial u}{\partial y}$, the z-component relative vorticity.

Terms $A$ through $F$ in (1) represent the horizontal vorticity advection, vertical vorticity advection, divergence, tilting, solenoidal and frictional terms, respectively. Among these terms, the frictional term ($F$) is generally one order of magnitude smaller than the other terms in (1) and will not be examined here. Likewise, the solenoidal term ($E$) requires retrieved information derived from

the Doppler wind and is subject to larger uncertainty; hence, it will not be treated here. The remaining terms ($A$ through $D$) can be determined from the three wind components and their spatial derivatives.

Similarly, the x- and y-component vorticity equation can also be obtained as follows:

$$\frac{\partial \xi}{\partial t} = -\vec{V}_h \cdot \vec{\nabla}_h \xi - w \frac{\partial \xi}{\partial z} - \xi \left(\vec{\nabla}_h \cdot \vec{V}_h + \frac{\partial w}{\partial z}\right) + Big(\xi \frac{\partial u}{\partial x} + \eta \frac{\partial u}{\partial y} + \zeta \frac{\partial u}{\partial z}\right) - \left(\frac{\partial \alpha}{\partial y}\frac{\partial p}{\partial z} - \frac{\partial \alpha}{\partial z}\frac{\partial p}{\partial y}\right) + \left(\frac{\partial fz}{\partial y} - \frac{\partial fy}{\partial z}\right) \tag{2}$$

$$\frac{\partial \eta}{\partial t} = -\vec{V}_h \cdot \vec{\nabla}_h \eta - w \frac{\partial \eta}{\partial z} - \eta \left(\vec{\nabla}_h \cdot \vec{V}_h + \frac{\partial w}{\partial z}\right) + \left(\xi \frac{\partial v}{\partial x} + \eta \frac{\partial v}{\partial y} + \zeta \frac{\partial v}{\partial z}\right) - \left(\frac{\partial \alpha}{\partial z}\frac{\partial p}{\partial x} - \frac{\partial \alpha}{\partial x}\frac{\partial p}{\partial z}\right) + \left(\frac{\partial fx}{\partial z} - \frac{\partial fz}{\partial x}\right) \tag{3}$$

Values of each term in (1)-(3) at every analysis level were determined from the Doppler derived winds using fourth-order finite differencing in horizontal and second-order finite differencing in vertical. The horizontal grid spacing used was 0.5 *km*, while the vertical grid spacing was 0.25 *km*.

## 4. DISCUSSION OF RESULTS

### 4.1 Complex Case: 5 August 1982

The analyzed vorticity field for 1845 MDT at the 0.5 *km* level in presented on the wind field in Figure 1. This storm is more complicated than the previous case of 14 July 1982 as depicted in Part II of this study. It produced a microburst, M1 (−2, −24), a gust front, northeast through southeast (dashed line) of M1, and an enhanced downdraft, M2 (−6, −19). The complex interactions of the flow fields of the enhanced downdraft and M1 combine to create a large elongated region of the two horizontal components of vorticity from (−7, −17) to (−2, −21). This area corresponds to an area of low perturbation pressure gradient (see Figure 8a in Part I), and is a feature found in horizontal vortex circulations (Kessinger *et al.* 1988). A circulation is not found here, but rather, the horizontal vorticity is high. The actual shear then is not apparent simply by examining the Doppler derived wind field. The microburst

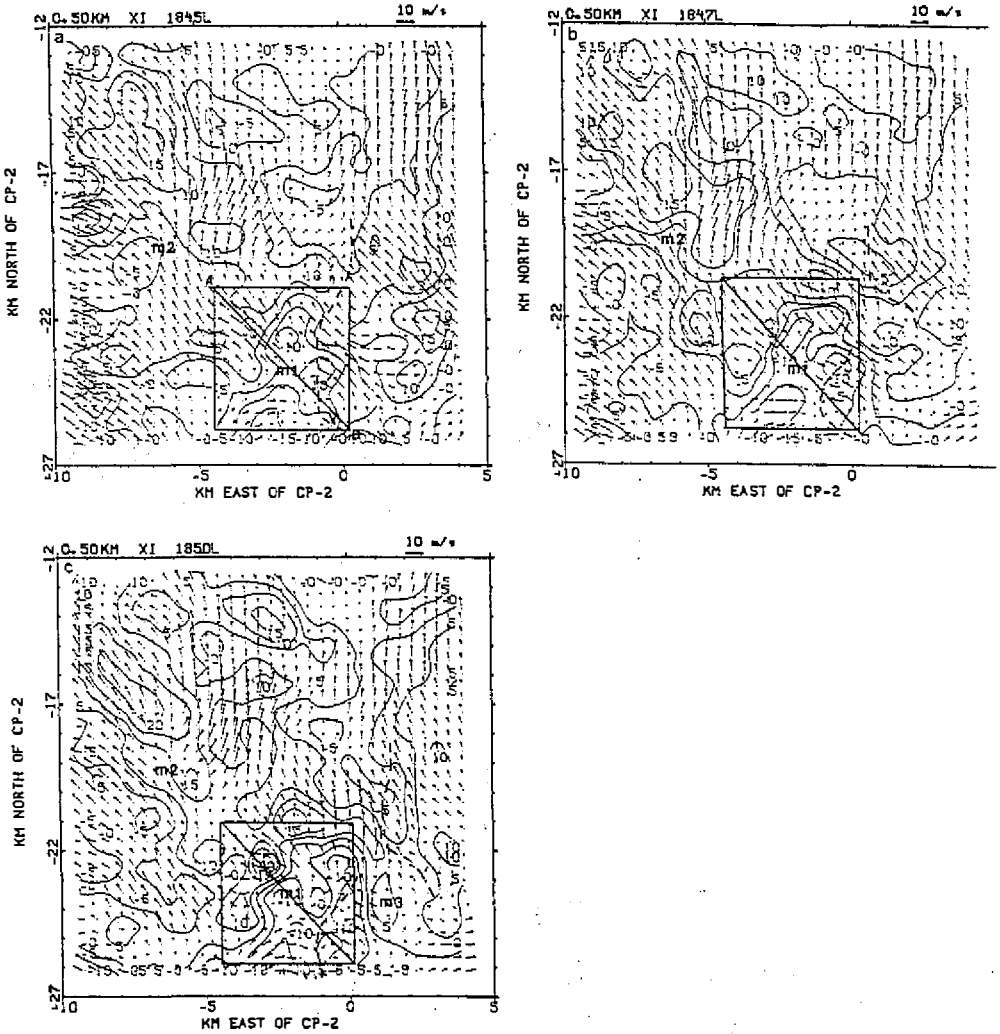


Fig. 1. Plan view of the horizontal wind field with $\xi$ vorticity superimposed at 0.5 *km* for (a) 1845, (b) 1847 and (c) 1850 MDT 5 August 1982. Distances are in kilometers from the CP-2 radar. Centers of microburst are denoted by a symbol M. The dashed line shows a microburst gust front. A box with dimensions of 5 *km* by 5 *km* indicates the microburst domain. Line AB in panel a signifies the northwest southeast cross section shown in Figure 2. Units are in $10^{-3}$ $s^{-1}$.

domain with horizontal dimensions of 5 *km* by 5 *km* (small box) encompassed M1, a large portion of the gust front, and the mesocyclone-like vortex *V*. The inflowing environment air is evident east of M1 at the bulge of the gust front.

Values of $\xi$ (Figure 1a) are overwhelmingly negative in the microburst domain at all levels with a pattern as shown here for 0.5 *km*. $\xi$ is positive to the northwest of M1 as depicted in the northwest-southeast cross section (see Figure 2a). Above 0.5 *km*, $\xi$ is positive in this northwest quadrant. It is in this region that the divergent outflow of M1 is strongest in the lowest levels.

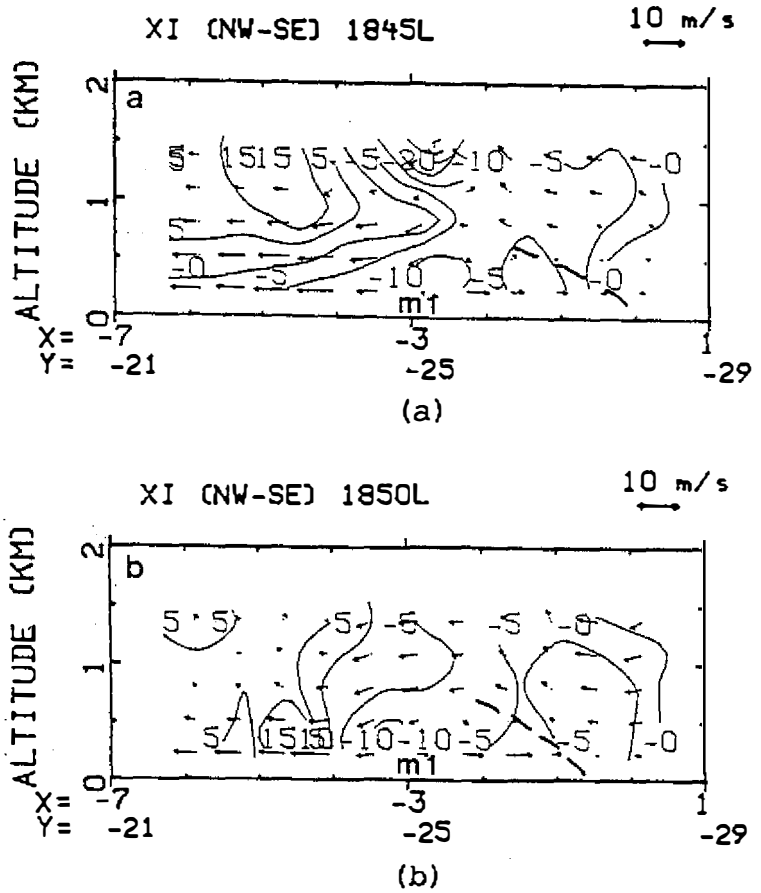


Fig. 2. Vertical cross section along line AB in Figure 1a showing the distribution of $\xi$ vorticity in relation to the wind field at (a) 1845 and (b) 1850 MDT 5 August 1982. Location of microburst M1 is indicated. Contour interval for $\xi$ is $5 \times 10^{-3}$ $s^{-1}$.

The reason for the distribution of $\xi$ as largely negative south of $M_1$ and positive north can be seen from Figure 2. The inflowing air velocity increases with height south of $M_1$, i.e., $\partial v/\partial z$ is positive and decreases strongly in the north. This results in the given 1845 MDT $\xi$ distribution. By 1850 MDT (Figure 2b), the only real change is the most shallow layer of maximum outflow winds to the north, i.e., $\partial v/\partial z$ is large negative and therefore, $\xi$ is large positive ($\partial w/\partial y$ is weak).

Values of $\xi$ change very little between 1845 and 1847 MDT (Figure 1b). From Tables 1~2 only a slight increase in the mean values of $\xi$ at low levels below 1 *km* over both domains and a decrease above 1 *km* is detected. Standard deviation values remain the same.

By 1850 MDT, $\xi$ continues virtually unchanged at 0.5 *km* (Figure 1c) except for the northwest quadrant of the microburst domain. Over the storm

Table 1. Area mean ($\langle\rangle$) and standard deviation (rms) values for each vorticity component over storm domain (15 $km \times 15$ $km$) for 1845, 1847 and 1850 MDT 5 August 1982. Units are in $10^{-3}$ $s^{-1}$.

1845 MDT

| Ht($km$) | $\langle\xi\rangle$ | $\xi_{rms}$ | $\langle\eta\rangle$ | $\eta_{rms}$ | $\langle\varsigma\rangle$ | $\varsigma_{rms}$ |
|---|---|---|---|---|---|---|
| 0.25 | 0.6 | 6.3 | −2.40 | 6.6 | 0.12 | 2.9 |
| 0.50 | 1.8 | 6.3 | −1.60 | 6.3 | 0.20 | 3.0 |
| 0.75 | 3.4 | 6.2 | −0.51 | 5.9 | 0.28 | 3.1 |
| 1.00 | 3.8 | 4.8 | −0.02 | 4.9 | 0.29 | 3.2 |
| 1.25 | 3.7 | 5.5 | 0.11 | 5.1 | 0.24 | 3.2 |

1847 MDT

| Ht($km$) | $\langle\xi\rangle$ | $\xi_{rms}$ | $\langle\eta\rangle$ | $\eta_{rms}$ | $\langle\varsigma\rangle$ | $\varsigma_{rms}$ |
|---|---|---|---|---|---|---|
| 0.25 | 1.7 | 6.3 | −1.50 | 6.8 | 0.15 | 3.1 |
| 0.50 | 2.6 | 6.2 | −1.30 | 6.4 | 0.19 | 3.2 |
| 0.75 | 3.8 | 6.2 | −0.95 | 5.9 | 0.26 | 3.3 |
| 1.00 | 3.4 | 5.2 | −0.95 | 3.6 | 0.32 | 3.4 |
| 1.25 | 2.7 | 6.0 | −1.10 | 2.4 | 0.19 | 3.7 |

1850 MDT

| Ht($km$) | $\langle\xi\rangle$ | $\xi_{rms}$ | $\langle\eta\rangle$ | $\eta_{rms}$ | $\langle\varsigma\rangle$ | $\varsigma_{rms}$ |
|---|---|---|---|---|---|---|
| 0.25 | 2.2 | 7.4 | −1.50 | 7.0 | 0.19 | 3.0 |
| 0.50 | 3.0 | 6.6 | −1.60 | 6.2 | 0.21 | 3.2 |
| 0.75 | 4.2 | 6.2 | −1.40 | 5.4 | 0.31 | 3.4 |
| 1.00 | 4.5 | 5.5 | −0.65 | 4.7 | 0.38 | 3.4 |
| 1.25 | 4.4 | 5.6 | −0.07 | 4.8 | 0.30 | 3.6 |

Table 2. Same as Table 1 except for the microburst domain (5 $km \times 5$ $km$).

1845 MDT

| Ht($km$) | $\langle\xi\rangle$ | $\xi_{rms}$ | $\langle\eta\rangle$ | $\eta_{rms}$ | $\langle\varsigma\rangle$ | $\varsigma_{rms}$ |
|---|---|---|---|---|---|---|
| 0.25 | −6.50 | 6.5 | −2.50 | 11.6 | 0.46 | 4.7 |
| 0.50 | −4.30 | 6.4 | −1.10 | 10.0 | 0.98 | 4.4 |
| 0.75 | −1.00 | 7.3 | 0.47 | 5.8 | 1.20 | 3.9 |
| 1.00 | 0.78 | 6.5 | 0.74 | 5.1 | 1.20 | 4.2 |
| 1.25 | 1.40 | 8.7 | 0.88 | 5.8 | 1.00 | 4.2 |

1847 MDT

| Ht($km$) | $\langle\xi\rangle$ | $\xi_{rms}$ | $\langle\eta\rangle$ | $\eta_{rms}$ | $\langle\varsigma\rangle$ | $\varsigma_{rms}$ |
|---|---|---|---|---|---|---|
| 0.25 | −4.50 | 6.1 | −3.30 | 9.4 | 0.49 | 4.9 |
| 0.50 | −3.80 | 6.1 | −3.20 | 9.4 | 1.17 | 4.8 |
| 0.75 | −1.60 | 7.7 | −1.70 | 8.4 | 1.34 | 4.6 |
| 1.00 | 0.08 | 7.7 | 1.30 | 4.6 | 1.26 | 4.4 |
| 1.25 | 0.43 | 8.9 | −1.00 | 2.9 | 1.59 | 4.7 |

1850 MDT

| Ht($km$) | $\langle\xi\rangle$ | $\xi_{rms}$ | $\langle\eta\rangle$ | $\eta_{rms}$ | $\langle\varsigma\rangle$ | $\varsigma_{rms}$ |
|---|---|---|---|---|---|---|
| 0.25 | −1.87 | 9.2 | −3.62 | 9.6 | 0.48 | 4.1 |
| 0.50 | −0.82 | 8.1 | −2.47 | 8.7 | 0.99 | 4.4 |
| 0.75 | 0.70 | 8.2 | −0.02 | 6.9 | 1.22 | 4.6 |
| 1.00 | 2.22 | 7.3 | 2.15 | 5.0 | 1.40 | 4.0 |
| 1.25 | 3.19 | 7.6 | 3.06 | 5.0 | 1.48 | 3.8 |

domain, the elongated region of strong $\xi$ values mentioned at 1845 MDT from north of M2, to north of M1 has intensified. A band of strong positive $\xi$ values $10 \times 10^{-3}\ s^{-1}$ to $20 \times 10^{-3}\ s^{-1}$ to $15 \times 10^{-3}\ s^{-1}$ lies was southwest to north of M1. The wind field in this region curves anticyclonically (at 0.5 $km$) emanating from the high perturbation pressure dome (0.2 $mb$) associated with M1 into a lower pressure region between both M1 and the high pressure dome associated with M2 (see Figure 8b in Part I).

Tables 1~2 show that at 1850 MDT $\xi$ increases in the area mean at all levels in the storm domain and microburst domain. In fact, the largely negative $\xi$ mean values at low levels that existed at 1845 and 1847 MDT have all but been reversed in the mean by 1850 MDT. This indicates the strengthening of a positive $\xi$ field as shown in Figure 1c northwest of M1. Figure 2 illustrates the stronger vertical shear at 1850 MDT responsible for the stronger positive $\xi$ values.

Table 3 lists the area mean and standard deviation values for each of the four budget terms in the storm domain. These four terms are horizontal vorticity advection (HAD), vertical vorticity advection (VAD), divergence (DIV) and tilting (TILT). At 1845 MDT, a balance must be accomplished between HAD and the combined effect of DIV and TILT since VAD is small. A balance is not met and by comparing vertical totals (see the last row in Tables 3~4 for each analysis time), a net increase of $\xi$ is suggested. By 1847 MDT, the contribution from VAD has increased slightly (level by level) but is still one order of magnitude smaller in the mean than the remaining terms. At this time, HAD and TILT acting positively (source) at low levels overwhelms the loss through DIV. Across each time period, it is apparent that the DIV term is the sole generator of negative $\xi$. The remaining terms generate positive $\xi$ with the strongest generation occurring below 0.75 $km$.

In the smaller microburst domain (Table 4), the area mean and standard deviation values are larger than at the storm domain (Table 3). From Figure 1a it is evident that due to the overwhelming negative $\xi$ field, HAD would act as a sink as the table indicates. VAD counters by acting as a source. TILT is a source at each time period with maximum contribution occurring at 1847 MDT. The large horizontal gradients of $\xi$ create a very strong HAD term leading to removal of positive $\xi$ within the microburst domain over time. VAD and TILT counteract this removal mechanism and dominate at 1845 and 1847 MDT. By 1850 MDT when the $\xi$ gradient is strongest, DIV acts with VAD and TILT to attempt a balance. As the $\xi$ field gets stronger, the DIV term especially to the north of $M_1$ becomes a strong source.

Between 1845 and 1850 MDT, $\langle\eta\rangle$ values remain predominantly negative (Tables. 1~2) over the storm domain and below 1 $km$ in the microburst domain. A tight gradient of $\eta$ results from the strong outflow of M1 eastward at low levels

Table 3. Area mean ($\langle\rangle$) and standard deviation ($\sigma$) values for the budget terms of $\xi$ vorticity over the storm domain (15 $km \times 15$ $km$) for 1845 , 1847 and 1850 MDT 5 August 1982. Units are in $10^{-6}$ $s^{-2}$. Physical meanings of the budget terms are given in the text.

1845 MDT

| Ht($km$) | ⟨HAD⟩ | HAD$_\sigma$ | ⟨VAD⟩ | VAD$_\sigma$ | ⟨DIV⟩ | DIV$_\sigma$ | ⟨TILT⟩ | TILT$_\sigma$ |
|---|---|---|---|---|---|---|---|---|
| 0.25 | 4.20 | 39.5 | 0.01 | 2.7 | −1.30 | 16.9 | 1.20 | 19.0 |
| 0.50 | 3.30 | 34.8 | 0.33 | 8.7 | −1.30 | 9.9 | 1.70 | 17.3 |
| 0.75 | 0.92 | 30.6 | 0.59 | 10.0 | −0.63 | 9.5 | −0.52 | 16.8 |
| 1.00 | −0.61 | 30.1 | 0.03 | 13.0 | 0.49 | 10.1 | −1.20 | 16.2 |
| 1.25 | −3.50 | 44.3 | −0.42 | 15.9 | 0.72 | 13.7 | −1.70 | 20.9 |
| TOTAL | 4.31 | | 0.54 | | −2.02 | | −0.52 | |

1847 MDT

| Ht($km$) | ⟨HAD⟩ | HAD$_\sigma$ | ⟨VAD⟩ | VAD$_\sigma$ | ⟨DIV⟩ | DIV$_\sigma$ | ⟨TILT⟩ | TILT$_\sigma$ |
|---|---|---|---|---|---|---|---|---|
| 0.25 | 4.30 | 45.1 | 0.15 | 2.6 | −1.70 | 14.6 | 2.30 | 20.3 |
| 0.50 | 2.80 | 36.8 | 0.53 | 8.9 | −1.30 | 12.1 | 2.20 | 17.5 |
| 0.75 | 0.60 | 33.8 | 0.63 | 11.0 | −0.94 | 11.4 | 1.20 | 17.1 |
| 1.00 | 1.20 | 29.9 | 0.46 | 15.5 | 0.21 | 10.2 | 0.15 | 10.5 |
| 1.25 | 1.60 | 35.5 | 0.51 | 19.4 | −0.94 | 11.3 | 0.94 | 18.9 |
| TOTAL | 10.50 | | 2.28 | | −4.67 | | 6.79 | |

1850 MDT

| Ht($km$) | ⟨HAD⟩ | HAD$_\sigma$ | ⟨VAD⟩ | VAD$_\sigma$ | ⟨DIV⟩ | DIV$_\sigma$ | ⟨TILT⟩ | TILT$_\sigma$ |
|---|---|---|---|---|---|---|---|---|
| 0.25 | 5.00 | 55.0 | 0.04 | 2.8 | −2.40 | 20.8 | 4.65 | 24.4 |
| 0.50 | 2.30 | 39.2 | −0.11 | 9.5 | −1.20 | 12.0 | 2.98 | 21.7 |
| 0.75 | −1.20 | 31.8 | −0.06 | 12.2 | 0.27 | 9.4 | −0.65 | 20.5 |
| 1.00 | −1.60 | 26.1 | 1.04 | 12.6 | 1.40 | 12.0 | −0.95 | 18.3 |
| 1.25 | −2.70 | 29.9 | 1.62 | 13.4 | 1.63 | 10.2 | −1.60 | 20.3 |
| TOTAL | 1.80 | | 2.53 | | −0.30 | | 4.43 | |

Table 4. Same as Table 3 except for the microburst domain (5 $km \times 5$ $km$).

1845 MDT

| Ht($km$) | ⟨HAD⟩ | HAD$_\sigma$ | ⟨VAD⟩ | VAD$_\sigma$ | ⟨DIV⟩ | DIV$_\sigma$ | ⟨TILT⟩ | TILT$_\sigma$ |
|---|---|---|---|---|---|---|---|---|
| 0.25 | −9.40 | 45.8 | 1.00 | 5.3 | 4.50 | 33.4 | −5.90 | 34.6 |
| 0.50 | −4.80 | 36.9 | 3.70 | 16.9 | −3.80 | 15.5 | 7.30 | 28.7 |
| 0.75 | −4.70 | 46.1 | 1.90 | 17.3 | −1.40 | 11.8 | 0.16 | 18.9 |
| 1.00 | 0.46 | 37.5 | −0.16 | 24.2 | −2.00 | 17.1 | 3.20 | 25.5 |
| 1.25 | 2.00 | 53.4 | 0.68 | 31.8 | −1.70 | 19.5 | 6.20 | 29.6 |
| TOTAL | −16.44 | | 7.12 | | −4.40 | | 10.96 | |

1847 MDT

| Ht($km$) | ⟨HAD⟩ | HAD$_\sigma$ | ⟨VAD⟩ | VAD$_\sigma$ | ⟨DIV⟩ | DIV$_\sigma$ | ⟨TILT⟩ | TILT$_\sigma$ |
|---|---|---|---|---|---|---|---|---|
| 0.25 | −6.40 | 66.7 | 0.46 | 5.1 | −0.39 | 26.1 | −1.70 | 32.7 |
| 0.50 | −11.00 | 58.8 | 2.49 | 15.9 | −1.79 | 18.5 | 0.43 | 26.5 |
| 0.75 | −11.60 | 56.9 | 6.02 | 16.3 | −2.16 | 15.7 | 3.22 | 22.4 |
| 1.00 | −4.00 | 56.1 | 4.94 | 20.0 | −1.14 | 17.6 | 5.61 | 27.7 |
| 1.25 | 0.96 | 67.4 | 2.35 | 25.2 | −3.39 | 24.4 | 8.85 | 38.2 |
| TOTAL | −32.04 | | 16.26 | | −8.87 | | 16.41 | |

1850 MDT

| Ht($km$) | ⟨HAD⟩ | HAD$_\sigma$ | ⟨VAD⟩ | VAD$_\sigma$ | ⟨DIV⟩ | DIV$_\sigma$ | ⟨TILT⟩ | TILT$_\sigma$ |
|---|---|---|---|---|---|---|---|---|
| 0.25 | −16.10 | 100.9 | 2.40 | 5.6 | 2.80 | 42.0 | 0.25 | 41.2 |
| 0.50 | −20.90 | 66.5 | 7.70 | 18.7 | 1.30 | 18.7 | 4.55 | 34.5 |
| 0.75 | −19.00 | 49.7 | 7.70 | 22.2 | 2.30 | 13.6 | 3.51 | 31.9 |
| 1.00 | −10.10 | 36.6 | 4.80 | 20.7 | 3.60 | 18.1 | 3.11 | 22.3 |
| 1.25 | −6.10 | 37.9 | 4.70 | 19.0 | 3.30 | 13.9 | 3.31 | 18.1 |
| TOTAL | −72.20 | | 27.30 | | 13.30 | | 14.73 | |

and the strong inflowing air especially east of M1. This helps locate the gust front associated with M1 at 1845 and 1847 MDT as well as a new gust front that develops at 1850 MDT associated with the M3 (Figure 3).

The most interesting changes for $\eta$ occur within the microburst domain as maximum positive and negative $\eta$ centers pivot around M1 and become oriented northwest to southeast through the center of M1 with positive $\eta$ to the northwest (Figure 3c). The tight horizontal gradient of $\eta$ values along the gust front weakens slightly with time and it appears in cross section (Figure 4) that the slope of the gust front is most shallow at 1850 MDT in fact approaching horizontal above and southeast of M1. This is to say that negative $\eta$ is being

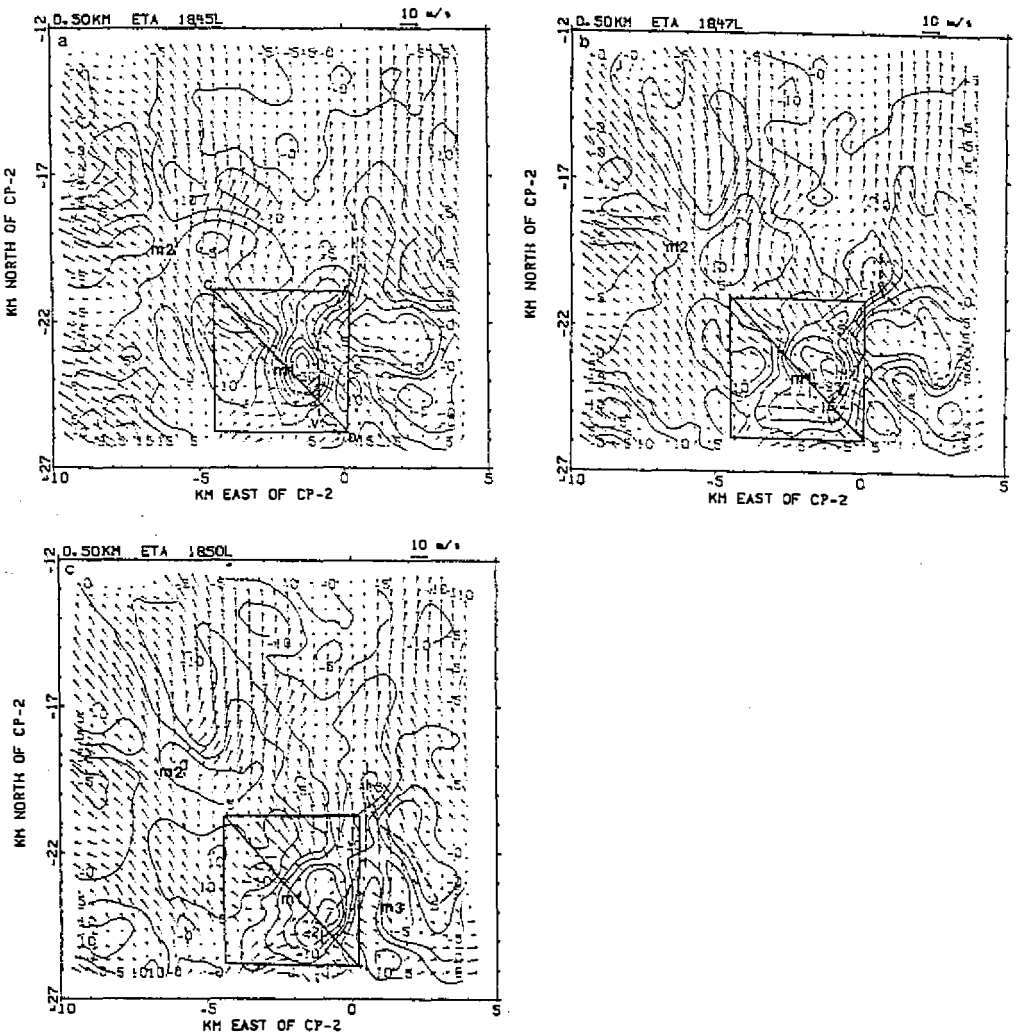


Fig. 3. As in Figure 1 except for $\eta$ vorticity. Line CD in panel a signifies the northwest-southeast cross section presented in Figure 4.

generated and is being spread out to the southeast at lower levels of the storm. Tables 1~2 show, especially in the microburst domain, that positive $\eta$ is being generated above 0.75 *km* and destroyed below 0.75 *km*.

The $\eta$ field in Figure 3a has its strongest negative value, $-32 \times 10^{-3}\ s^{-1}$, at this level (0.5 *km*) just east of M1. The gust front is closest to M1 at this point. The $\eta$ field parallels if not defines the location of the gust front with its very tight gradient adjacent to the gust front. Table 5 shows the budget terms for $\eta$ over the microburst domain. It is seen that HAD and VAD and likewise, DIV and TILT act, in general, to oppose each other.

Figure 5 shows the $\zeta$ field in plan view at 0.5 *km*, and Tables 1~2 list the area means standard deviations by level for both domains. From Table 1, it is apparent that $\zeta$ changes very little statistically at the storm domain. The largest changes occur in the microburst domain.

From Figure 5a, two areas of positive $\zeta$ are evident. One area west of M1 ($\zeta > 4 \times 10^{-3}\ s^{-1}$) at 0.5 *km* and the other along the gust front with a maximum ($14 \times 10^{-3}\ s^{-1}$) associated with the mesocyclonic-like vortex, $V$, located at the southern end of this gust front at 1845 MDT.

By 1847 MDT (Figure 5b), the area along the gust front has been split as $\zeta$ is diminished just south of M1 and this continues at 1850 MDT (Figure 5c). The mesocyclone-like vortex, $V$, weakens with time. The area of $\zeta$ greater than $12 \times 10^{-3}\ s^{-1}$ tracks northwestward with time, weakens as it approaches M1, and merges with the positive $\zeta$ area to the west of M1.

A west-east cross section (Figure 6) shows that initially the area west of M1 is shallow extending only up to 0.5 *km*. By 1847 MDT and continuing at 1850 MDT, this area experiences a spin up of vorticity from the top down. A new misocyclone, C1, develops here by 1850 MDT with maximum $\zeta$ vorticity ($14 \times 10^{-3}\ s^{-1}$) occurring at 1.25 *km*.

A value of $\zeta$ has a maximum, $14 \times 10^{-3}\ s^{-1}$, in the mesocyclone-like vortex ($V$) and is positive along the gust front. Another region of positive $\zeta$ values is located west of M1. The west-east cross section through the microburst domain in Figure 6a indicates that the positive area west of M1 is a low-level feature, while the area along the gust front extends through several levels and slopes westward with height, i.e., with the updraft in this area. In the column directly above M1, $\zeta$ is negative below 0.75 *km* and positive above although the values are relatively small, i.e., near zero throughout. This signifies that the flow is largely irrotational through the horizontal plane.

Table 1 lists the area mean and standard deviation values for each component of vorticity by level for the storm domain. By comparing area mean values of $\xi$, $\eta$ and $\zeta$, it is seen that $\xi$ and $\zeta$ are predominantly positive over the storm domain with the strongest values above 0.5 *km*. Conversely, $\eta$ has

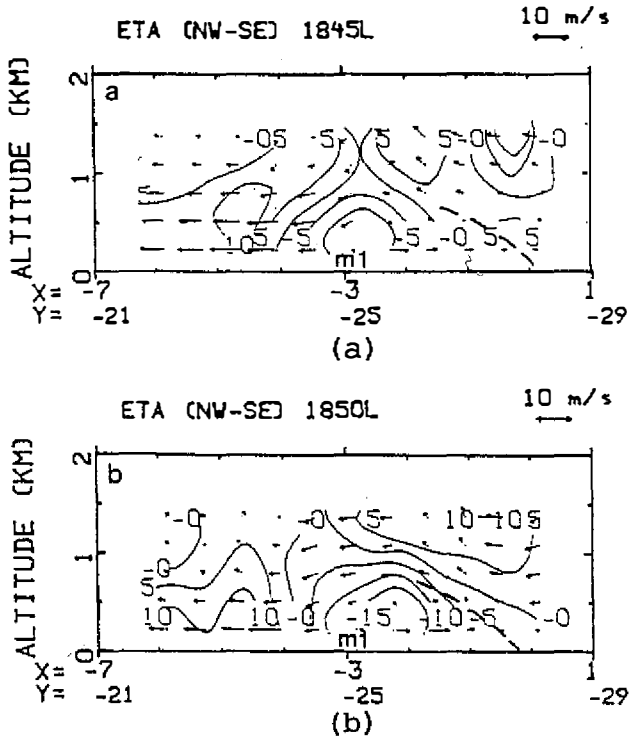


Fig. 4. As in Figure 2 except for $\eta$ vorticity.

Table 5. Area mean ($\langle\rangle$) and standard deviation ($\sigma$) values for the budget terms of $\eta$ vorticity over the microburst domain (5 $km \times 5$ $km$) for 1845, 1847 and 1850 MDT 5 August 1982. Units are in $10^{-6}$ $s^{-2}$.

1845 MDT

| Ht($km$) | ⟨HAD⟩ | HAD$_\sigma$ | ⟨VAD⟩ | VAD$_\sigma$ | ⟨DIV⟩ | DIV$_\sigma$ | ⟨TILT⟩ | TILT$_\sigma$ |
|---|---|---|---|---|---|---|---|---|
| 0.25 | 11.50 | 56.1 | −0.19 | 4.2 | −0.32 | 48.2 | −0.23 | 40.1 |
| 0.50 | 13.90 | 60.5 | −1.90 | 16.9 | −2.20 | 14.1 | 1.90 | 30.5 |
| 0.75 | 9.00 | 53.9 | −4.30 | 28.3 | −1.80 | 10.2 | 3.60 | 24.4 |
| 1.00 | 0.82 | 37.6 | −2.10 | 23.4 | −0.80 | 12.1 | 3.90 | 22.3 |
| 1.25 | −4.20 | 37.4 | 0.64 | 16.6 | 0.22 | 9.8 | 0.90 | 24.3 |
| TOTAL | 31.02 | | −7.85 | | −4.90 | | 10.07 | |

1847 MDT

| Ht($km$) | ⟨HAD⟩ | HAD$_\sigma$ | ⟨VAD⟩ | VAD$_\sigma$ | ⟨DIV⟩ | DIV$_\sigma$ | ⟨TILT⟩ | TILT$_\sigma$ |
|---|---|---|---|---|---|---|---|---|
| 0.25 | 0.79 | 50.1 | −0.25 | 5.7 | 3.50 | 39.2 | −16.50 | 40.8 |
| 0.50 | 6.64 | 59.5 | −0.02 | 18.5 | 1.30 | 27.4 | −6.50 | 29.9 |
| 0.75 | 5.23 | 62.7 | 3.36 | 24.0 | −1.80 | 21.0 | 3.70 | 26.9 |
| 1.00 | 3.75 | 51.6 | 2.71 | 26.9 | −1.70 | 10.4 | 8.80 | 23.8 |
| 1.25 | 1.95 | 35.7 | −0.33 | 27.1 | −1.40 | 8.4 | 8.00 | 32.0 |
| TOTAL | 18.36 | | 5.47 | | −0.10 | | −2.50 | |

1850 MDT

| Ht($km$) | ⟨HAD⟩ | HAD$_\sigma$ | ⟨VAD⟩ | VAD$_\sigma$ | ⟨DIV⟩ | DIV$_\sigma$ | ⟨TILT⟩ | TILT$_\sigma$ |
|---|---|---|---|---|---|---|---|---|
| 0.25 | −14.30 | 46.5 | 2.00 | 5.2 | 5.10 | 35.7 | −8.00 | 38.2 |
| 0.50 | −9.00 | 44.6 | 6.20 | 18.5 | 5.70 | 22.5 | −7.00 | 31.2 |
| 0.75 | −0.41 | 29.8 | 4.70 | 29.8 | −0.33 | 11.9 | 4.10 | 28.5 |
| 1.00 | −0.34 | 26.9 | −0.61 | 26.9 | −0.25 | 10.3 | 5.30 | 22.3 |
| 1.25 | −3.10 | 19.2 | −0.71 | 19.2 | 1.89 | 9.3 | 3.10 | 20.7 |
| TOTAL | −27.15 | | 11.58 | | 12.11 | | −2.50 | |

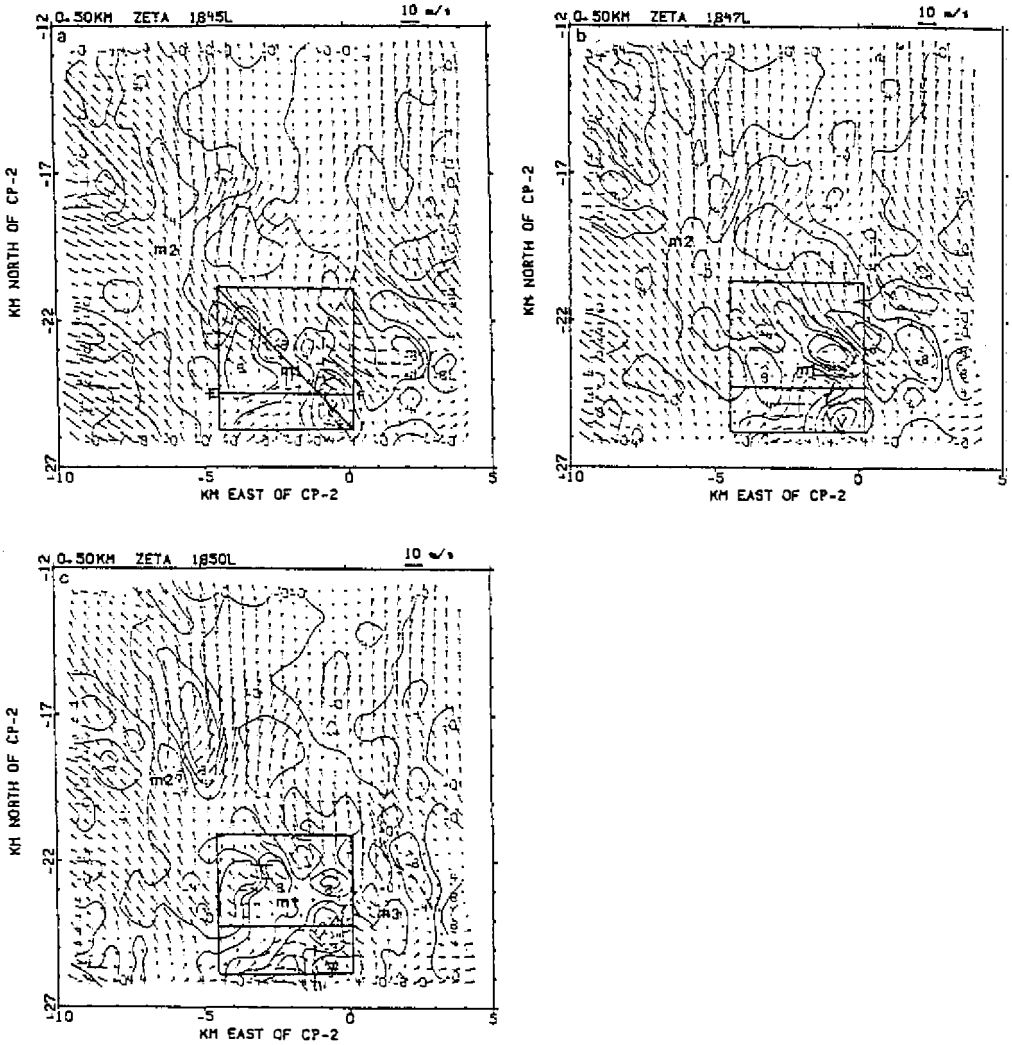


Fig. 5. As in Figure 1 except for $\varsigma$ vorticity. Line EF in panel a signifies the west-east cross section shown in Figure 6.

negative values at most levels. In the microburst domain (Table 2), $\xi$ and $\eta$ are predominantly negative in the mean below 0.75 $km$ ($\xi$) and 0.5 $km$ ($\eta$), while $\varsigma$ continues to be positive throughout with the larger mean values at the higher levels of the microburst domain.

The $\varsigma$ budget terms in the storm domain for virtually all times were found to be less than those in the microburst domain. Area mean values were typically on the order of $1 \times 10^{-7}$ $s^{-2}$ in the storm domain and $1 \times 10^{-6}$ $s^{-2}$ in the microburst domain, indicating the many more complex and opposing interactions at he storm domain. Typical values, while being of the same order in both domains, were larger in the microburst domain and extended through more depth.

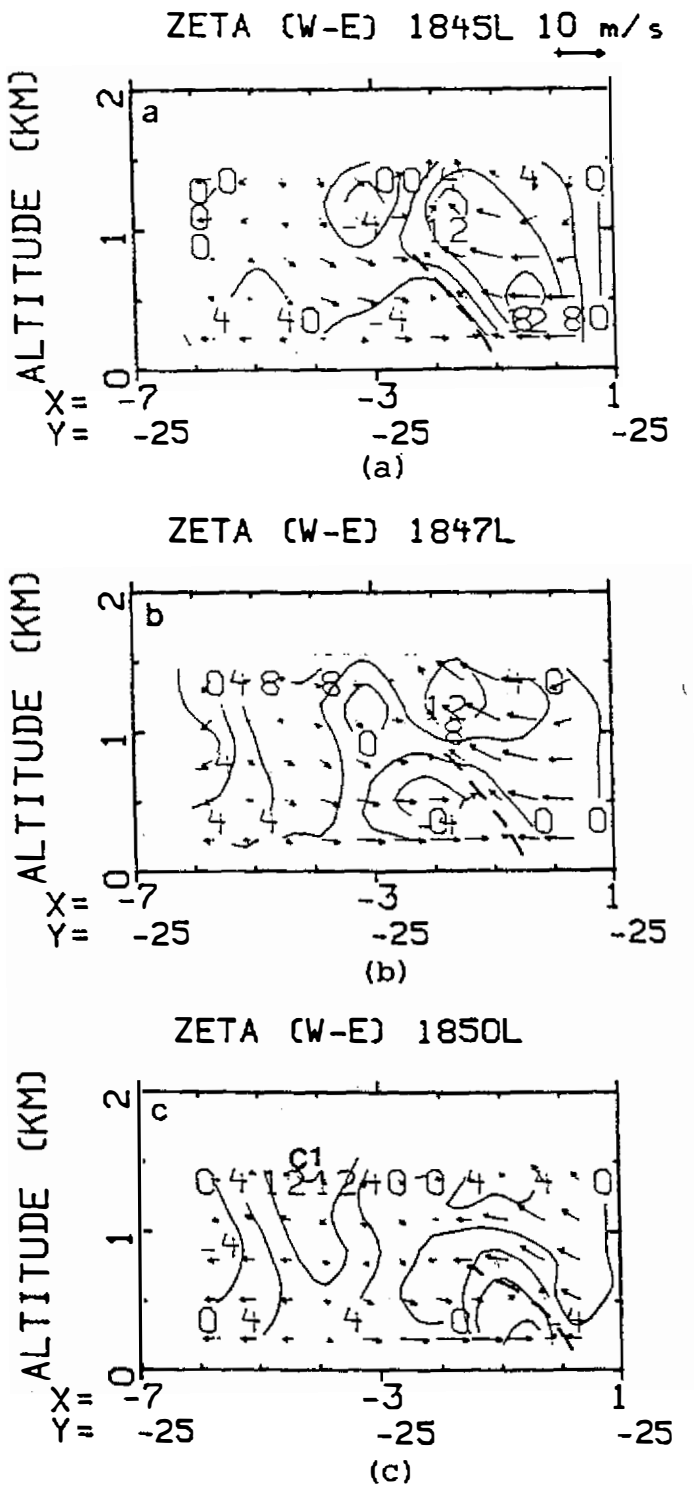


Fig. 6. Vertical cross section along line EF in Figure 5a showing the distribution of $\zeta$ vorticity in relation to the wind field at (a) 1845, (b) 1847 and (c) 1850 MDT 5 August 1982. Loxations of C1 and the gust front (dashed line) are indicated. Contour interval for $\zeta$ is $4 \times 10^{-3}$ $s^{-1}$.

The microburst domain $\zeta$ budget terms are presented in Table 6 for all analysis times. As noted earlier, the last row is a vertical total of the area means of each term. This provides a look at which terms act as a source or sink for $\zeta$. It can be seen that DIV and TILT become important, especially at 1847 and 1850 MDT at 0.75 *km* to 1.25 *km*. Both of these terms act positively to generate $\zeta$. So it appears that the contribution from DIV is critical to the formation and development of the misocyclone.

Horizontal variations of $\zeta$ at 1.25 *km* for all three analysis times are presented in Figure 7. Two misocyclones are evident; C1 is located to the west to southwest of M1, while C2 is located to the immediate east to northeast of M2. Centers of the misocyclones coincide with the maxima of $\zeta$ vorticity. For misocyclone C1, values of $\zeta$ increase from $8 \times 10^{-3}$ to $12 \times 10^{-3}$ $s^{-1}$ with a maximum of $12 \times 10^{-3}$ $s^{-1}$ at 1850 MDT (Figure 7c). Vertical vorticity advection (VAD) and divergence (DIV) terms contribute positive $\zeta$ at this level. On the other hand, misocyclone C2 begins to develop at 1847 MDT (Figure 7b) reaching the maximum intensity by 1850 MDT (Figure 7c). The circulation center coincides with a maximum value of $12 \times 10^{-3}$ $s^{-1}$. As discussed in Part I of

Table 6. Same as Table 5 except for $\zeta$.

1845 MDT

| Ht(*km*) | ⟨HAD⟩ | $HAD_\sigma$ | ⟨VAD⟩ | $VAD_\sigma$ | ⟨DIV⟩ | $DIV_\sigma$ | ⟨TILT⟩ | $TILT_\sigma$ |
|---|---|---|---|---|---|---|---|---|
| 0.25 | −1.80 | 28.6 | 0.23 | 3.4 | 4.90 | 14.4 | 1.80 | 9.4 |
| 0.50 | 2.80 | 30.3 | 1.50 | 8.5 | −0.03 | 7.9 | −0.85 | 11.6 |
| 0.75 | 1.90 | 26.9 | 1.99 | 15.2 | −0.30 | 8.4 | −2.10 | 13.9 |
| 1.00 | 0.54 | 28.6 | 2.10 | 11.2 | 0.36 | 10.1 | −1.30 | 15.4 |
| 1.25 | −1.90 | 24.1 | 2.10 | 22.7 | 1.70 | 7.0 | −0.83 | 24.8 |
| TOTAL | 1.54 | | 7.92 | | 6.63 | | −3.28 | |

1847 MDT

| Ht(*km*) | ⟨HAD⟩ | $HAD_\sigma$ | ⟨VAD⟩ | $VAD_\sigma$ | ⟨DIV⟩ | $DIV_\sigma$ | ⟨TILT⟩ | $TILT_\sigma$ |
|---|---|---|---|---|---|---|---|---|
| 0.25 | 4.90 | 36.8 | −0.13 | 3.9 | −0.75 | 16.5 | −1.90 | 12.6 |
| 0.50 | 5.70 | 27.0 | −0.58 | 9.4 | −2.26 | 9.1 | −1.60 | 16.4 |
| 0.75 | 0.92 | 30.9 | −2.61 | 13.9 | 0.16 | 9.5 | 1.90 | 16.6 |
| 1.00 | −4.75 | 27.9 | −1.58 | 10.5 | 2.67 | 10.3 | 4.50 | 13.3 |
| 1.25 | −6.50 | 26.1 | 0.45 | 14.4 | 4.00 | 9.3 | 4.60 | 16.2 |
| TOTAL | 0.27 | | −4.45 | | 3.82 | | 7.50 | |

1850 MDT

| Ht(*km*) | ⟨HAD⟩ | $HAD_\sigma$ | ⟨VAD⟩ | $VAD_\sigma$ | ⟨DIV⟩ | $DIV_\sigma$ | ⟨TILT⟩ | $TILT_\sigma$ |
|---|---|---|---|---|---|---|---|---|
| 0.25 | 8.39 | 34.5 | −0.11 | 4.89 | −4.40 | 15.8 | −3.10 | 11.1 |
| 0.50 | 4.94 | 38.2 | −1.46 | 10.20 | −1.70 | 11.4 | −1.30 | 14.5 |
| 0.75 | −0.06 | 32.9 | −2.91 | 13.30 | −0.84 | 7.6 | 2.40 | 12.5 |
| 1.00 | −4.76 | 21.6 | 0.22 | 12.50 | 2.41 | 8.0 | 1.60 | 15.5 |
| 1.25 | −5.50 | 15.4 | 3.62 | 14.40 | 3.38 | 6.3 | −1.50 | 19.0 |
| TOTAL | 3.01 | | −0.64 | | −1.15 | | −1.90 | |

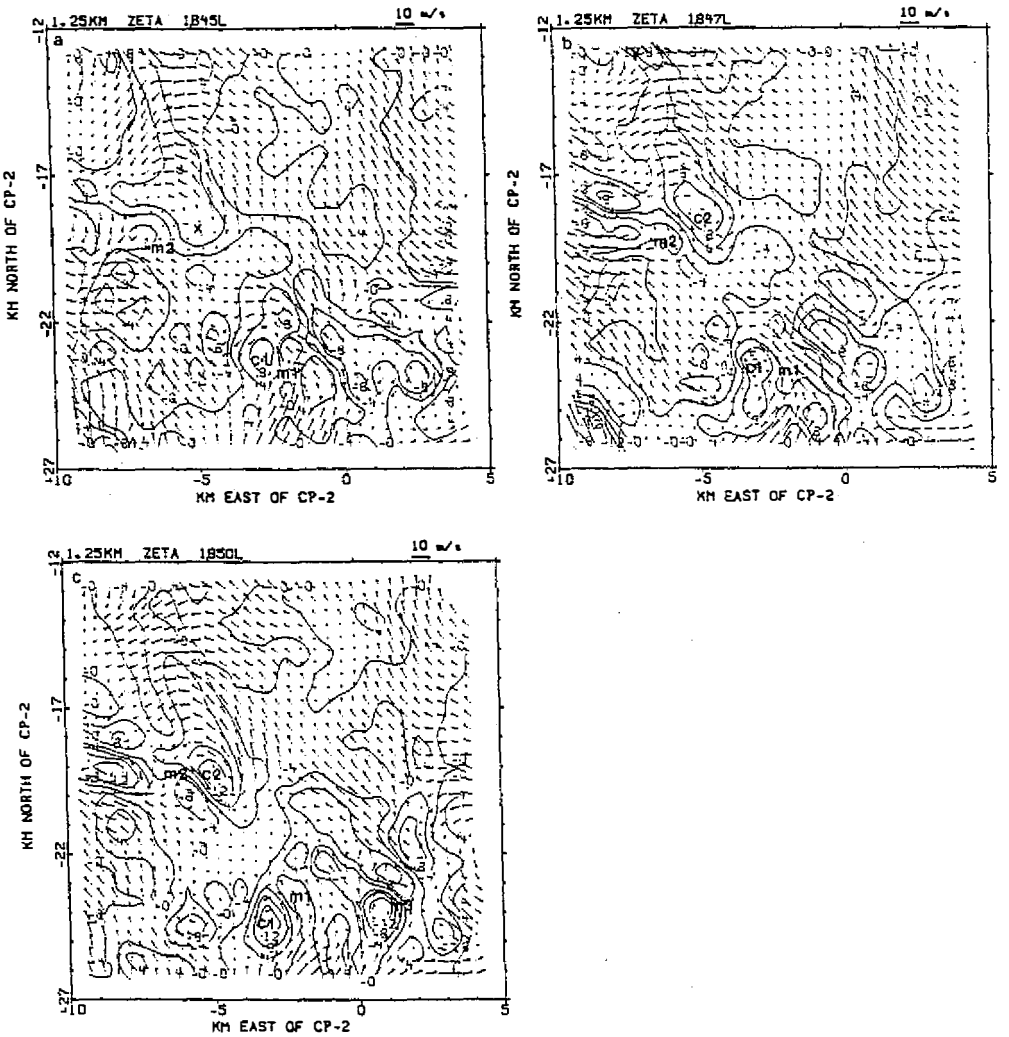


Fig. 7. Horizontal winds with $\zeta$ vorticity contours superimposed at 1.25 *km* for (a) 1845, (b) 1847 and (c) 1850 MDT 5 August 1982. Centers of microbursts (M1 and M2) and misocyclones (C1 and C2) are indicated Contour interval for $\zeta$ is $4 \times 10^{-3}\ s^{-1}$.

this study, the presence of misocyclones in the upper part of the atmospheric boundary layer is closely related to the structure and internal dynamics of the microburst.

## 4.2 The Simple Case: 14 July 1982

For brevity only the results at 1647 MDT 14 July 1982 are presented below. Figure 8 shows the contoured vorticity analysis for each vorticity component with horizontal wind vectors superimposed at 0.5 *km*. A gust front is denoted by a dashed line to the northwest of the microburst center ($M$). The

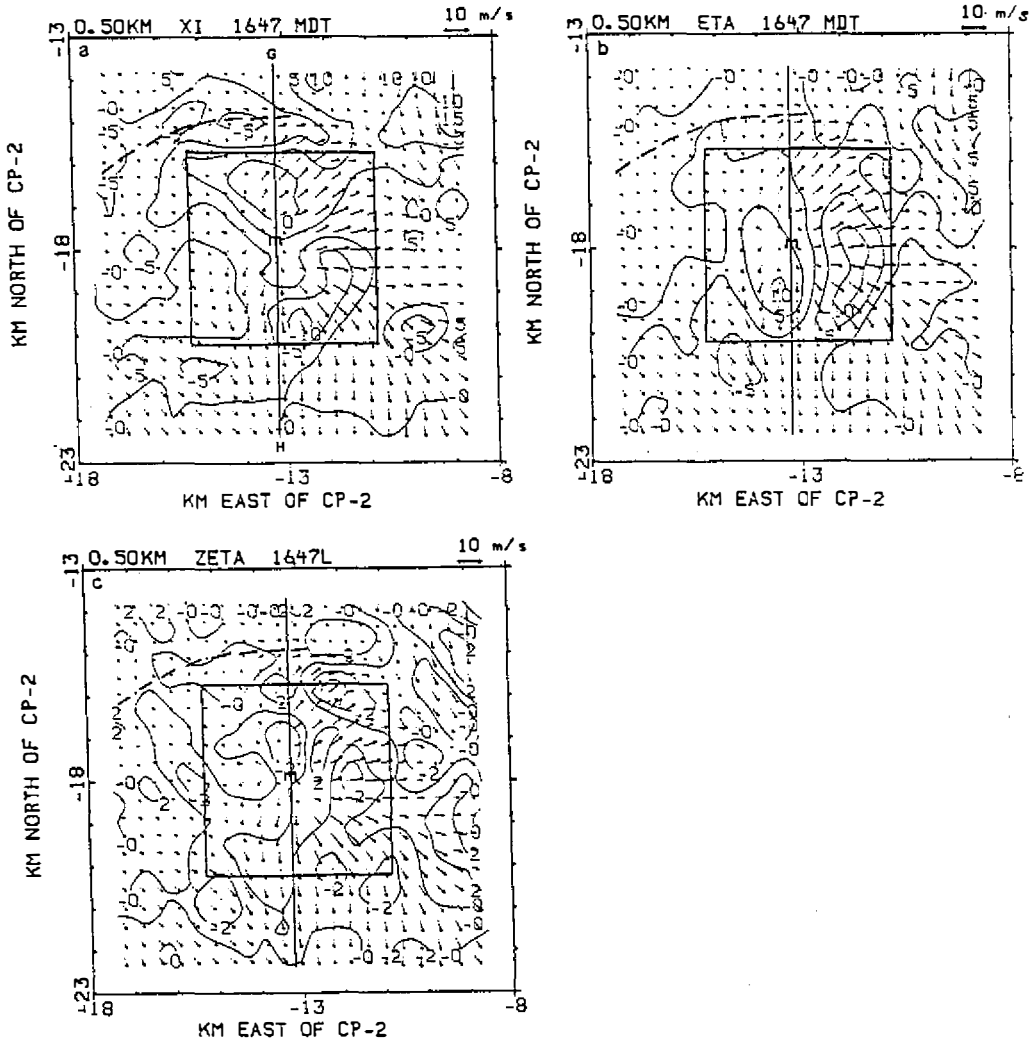


Fig. 8. Plan view of the horizontal wind field and isopleths for (a) $\xi$, (b) $\eta$ and (c) $\zeta$ at 0.5 *km* for 1647 MDT 14 July 1982. Distances are in kilometers from the CP-2 radar. Loxations of microburst ($M$) and gust front (dashed line) are indicated. The microburst domain (5 *km* × 5 *km*) is represented by a box. Line GH in panel a signifies the north-south cross section shown in Figure 9.

microburst domain is represented by a small box (5 *km* × 5 *km*). Note that $\xi$ has positive values north of the microburst and negative to the south (Figure 8a). The largest horizontal gradient of $\xi$ occurs across the gust front to the northwest. The analyzed $\eta$ field (Figure 8b), on the other hand, has the largest positive (negative) values on the west (east) side of the microburst. Values of the vertical vorticity component (Figure 8c) are relatively smaller than those of horizontal components in most areas. In the inner core region of the microburst, $\zeta$ is very small indicative of the diverging flow in this region as depicted in the study by Lin and Hughes (1987).

A north-south cross section along line GH in Figure 8a showing spatial variations of vorticities is presented in Figure 9. Note that a rotor (vortex circulation), located at ($y = -15.5$; $z = 0.75$), is apparent in the wind field on the microburst side of the gust front (Figure 9a). Its position coincides with a maximum value of $\xi$ ($18 \times 10^{-3}$ $s^{-1}$). On the south side of the microburst, the rotor is non-existent although the flow field does show a circulation, but it is not closed. Notice that the horizontal outflow to the north of $M$ is going against the environmental flow, while the outflow to the south is almost in the same direction as the environmental flow. For the $\eta$ field (Figure 9b), large positive values (up to $10^{-2}$ $s^{-1}$) occur in the region south of $M$ ($y = -19.5$; $z = 0.75$). Values of $\eta$ are relatively small over the north region. The vertical vorticity component (Figure 9c), in general, is much smaller than the horizontal components in the layer below 1 *km*. In this microburst-dominating layer, the horizontal diverging flow prevails and vorticity vectors are nearly horizontal.

Figure 10a depicts horizontal vorticity vectors at 0.75 *km*. Notice that a vortex ring surrounds the microburst center ($M$) indicative of the strong shear in this region. The field of perturbation pressure ($P'_d$) in relation to horizontal vorticity vectors at 0.75 *km* is illustrated in Figure 10b. It is evident that the vortex ring lies in a region of low pressure which serves to accelerate the wind. Likewise, the rotor itself is within the low pressure region as viewed in the north-south cross section (Figure 9d). Parsons *et al.* (1987), Droegemeier and Wilhelmson (1987) and Kessinger *et al.* (1988) also suggested that these vortex circulations could be partly responsible for the observed high surface winds.

The vortices studied by Kessinger *et al.* (1988) move away from the storm center. They hypothesized that variations in the strength of the downdraft may create separate centers of horizontal vorticity which then move down and away from the storm. The existence of vortices can be inferred from Figure 9 on either side of the microburst. The vorticity centers are more evident in southwest-northeast cross section (not shown). Time resolution does not allow tracking of these vorticity centers, but some movement down and outward can be inferred between 1647 MDT northeast of the microburst. This apparent movement could be a establishment or a development of vorticity lower and further away as opposed to actual movement.

In order to determine typical magnitudes of the three vorticity components, area means and standard deviations were computed over the full storm domain and the microburst domain, see a box in Figure 8. Findings are presented in Table 7. A comparison of standard deviations in the table shows that the $\xi$ and $\eta$ components are the dominant components at every level. Mean values of $\xi$ are positively large in the layer between 0.5 *km* and 1.5 *km*, while mean values of $\eta$ are negative from the surface to 2 *km*. The rotor, which af-

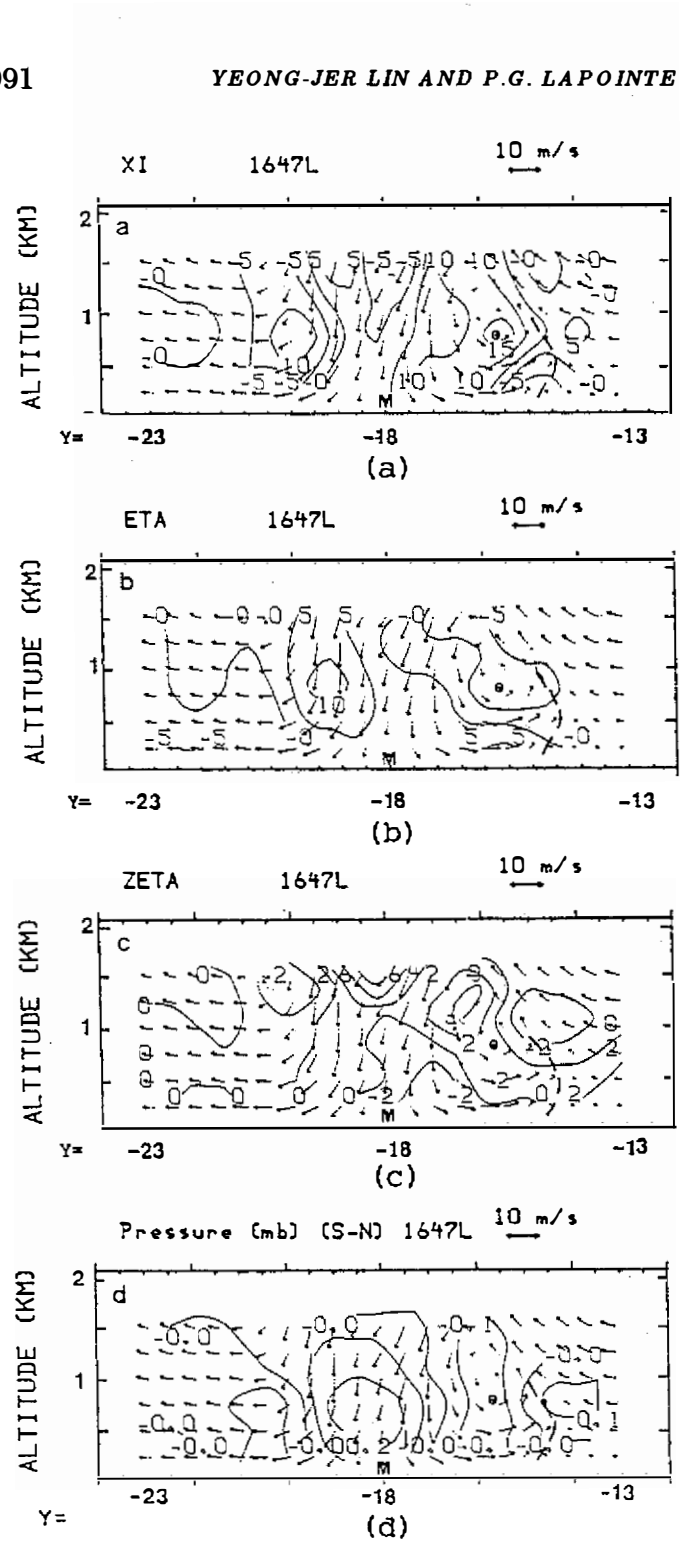


Fig. 9. Vertical cross section along line GH in Figure 8a showing the distributions of vorticity and perturbation pressure ($P_d'$) in relation to the wind field for (a) $\xi$, (b) $\eta$, (c) $\zeta$ and (d) $P_d'$ at 1647 MDT 14 July 1982. Gust front (dashed line), rotor ($O$) and microburst ($M$) are indicated. Contour interval for $P_d'$ is 0.1 $mb$, while contour intervals for $\xi$, $\eta$ and $\zeta$ are $5 \times 10^{-3}$, $5 \times 10^{-3}$ and $2 \times 10^{-3}$ $s^{-1}$, respectively.

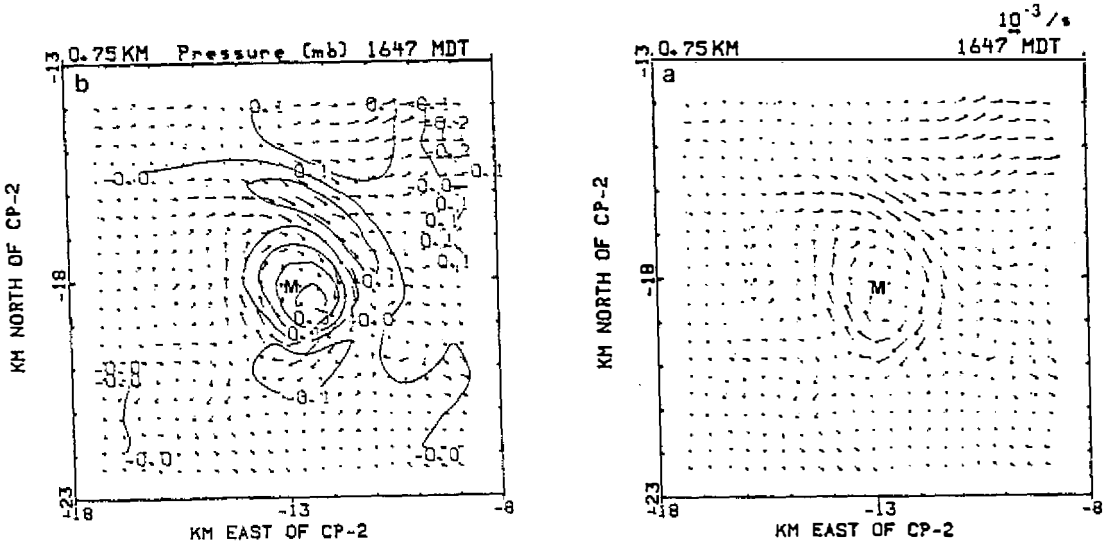


Fig. 10. Plan view of (a) horizontal vorticities ($\vec{i}\,\xi + \vec{j}\,\eta$) and (b) horizontal vorticities with $P'_d$ contours superimposed at 0.75 *km* for 1647 MDT 14 July 1982. The microburst center ($M$) is indicated. Contour interval for $P'_d$ is 0.1 *mb* (10 Pa).

Table 7. Area mean ($\langle\rangle$) and standard deviation (rms) values for each vorticity component over the storm domain (10 *km* × 10 *km*) and microburst domain (5 *km* × 5 *km*) for 1647 MDT 14 July 1982. Units are in $10^{-3}$ $s^{-1}$.

STORM ( × $10^{-4}$ $s^{-1}$ )

| Ht(*km*) | $\langle\xi\rangle$ | $\xi_{rms}$ | $\langle\eta\rangle$ | $\eta_{rms}$ | $\langle\varsigma\rangle$ | $\varsigma_{rms}$ |
|---|---|---|---|---|---|---|
| 0.25 | −1.8 | 45.6 | −3.5 | 29.0 | 0.87 | 15.6 |
| 0.50 | 13.5 | 46.5 | −1.4 | 33.3 | −0.22 | 14.9 |
| 0.75 | 28.5 | 50.5 | −1.8 | 47.4 | −1.90 | 14.4 |
| 1.00 | 19.8 | 40.7 | −3.8 | 42.5 | −1.90 | 17.1 |
| 1.50 | 3.5 | 41.4 | −2.9 | 38.9 | −0.06 | 19.9 |
| 2.00 | −6.5 | 43.6 | −0.4 | 38.1 | 1.40 | 22.9 |

MICROBURST ( × $10^{-4}$ $s^{-1}$ )

| Ht(*km*) | $\langle\xi\rangle$ | $\xi_{rms}$ | $\langle\eta\rangle$ | $\eta_{rms}$ | $\langle\varsigma\rangle$ | $\varsigma_{rms}$ |
|---|---|---|---|---|---|---|
| 0.25 | 9.9 | 46.7 | −3.20 | 34.3 | −0.60 | 15.9 |
| 0.50 | 18.4 | 50.5 | −4.60 | 47.5 | −3.50 | 14.6 |
| 0.75 | 24.6 | 68.6 | −0.95 | 77.1 | −2.70 | 13.2 |
| 1.00 | 21.2 | 55.7 | 3.60 | 64.0 | −0.45 | 19.3 |
| 1.50 | 16.5 | 53.3 | −0.48 | 53.1 | 1.20 | 24.0 |
| 2.00 | 10.7 | 53.8 | −7.80 | 47.8 | 5.00 | 31.1 |

fects the vorticity field at levels between 0.5 *km* and 1 *km*, and the predominant northerly flow to the northeast produce strong positive values for the $\xi$ area means at these levels. The values for $\eta$ and $\varsigma$ are more varied, positively and negatively, and hence their areal means are smaller than that of $\xi$.

The same results hold for the microburst domain with the exception that the $\eta$ component is strongest at levels between 0.75 $km$ and 1 $km$. Comparing across the domains, one finds the maximum positive and maximum negative values of each component over the grid, which illustrates the significance of the presence of the microburst, i.e., these values occur in the microburst domain predominantly.

Table 8 lists the results of the computed values of the terms in each of the component equations. It provides a level by level analysis of the areal means and standard deviations for each of the four terms, horizontal advection (HAD), vertical advection (VAD), divergence (DIV), and tilting (TILT) for the storm domain.

Since the area means for each component of the $\xi$, $\eta$ and $\zeta$ are at least one order of magnitude smaller than their standard deviations at each level,

Table 8. Area mean ($\langle\rangle$) and standard deviation ($\sigma$) values for the budget terms of three vorticity components ( $\xi$, $\eta$, $\zeta$) over the storm domain (10 $km \times$ 10 $km$) for 1647 MDT 14 July 1982. Units are in $10^{-6}$ $s^{-2}$.

X-COMPONENT

| Ht($km$) | $\langle$HAD$\rangle$ | HAD$_\sigma$ | $\langle$VAD$\rangle$ | VAD$_\sigma$ | $\langle$DIV$\rangle$ | DIV$_\sigma$ | $\langle$TILT$\rangle$ | TILT$_\sigma$ |
|---|---|---|---|---|---|---|---|---|
| 0.25 | 1.90 | 22.8 | −2.20 | 11.2 | 0.25 | 4.10 | 0.33 | 8.2 |
| 0.50 | 0.93 | 21.4 | −4.90 | 19.6 | 0.19 | 3.70 | −0.04 | 9.2 |
| 0.75 | −0.60 | 24.1 | −1.00 | 15.1 | −0.02 | 3.30 | −0.07 | 8.1 |
| 1.00 | 0.02 | 24.1 | 4.40 | 17.0 | 0.09 | 3.40 | 0.84 | 6.4 |
| 1.50 | −0.22 | 29.2 | 2.30 | 13.4 | −0.15 | 3.50 | 0.08 | 7.4 |
| 2.00 | −1.10 | 29.6 | 2.50 | 10.2 | 0.02 | 3.90 | 0.05 | 9.8 |
| TOTAL | 0.93 | | 1.10 | | 0.38 | | 1.19 | |

Y-COMPONENT

| Ht($km$) | $\langle$HAD$\rangle$ | HAD$_\sigma$ | $\langle$VAD$\rangle$ | VAD$_\sigma$ | $\langle$DIV$\rangle$ | DIV$_\sigma$ | $\langle$TILT$\rangle$ | TILT$_\sigma$ |
|---|---|---|---|---|---|---|---|---|
| 0.25 | 0.19 | 14.9 | 0.64 | 8.4 | 0.08 | 2.70 | −0.54 | 7.9 |
| 0.50 | 0.38 | 20.7 | 1.40 | 15.6 | 0.09 | 2.10 | −1.20 | 10.7 |
| 0.75 | 1.70 | 25.2 | 0.79 | 13.7 | −0.07 | 2.20 | −1.30 | 11.2 |
| 1.00 | 1.90 | 20.8 | −1.30 | 13.4 | −0.55 | 3.20 | 0.76 | 7.9 |
| 1.50 | 0.00 | 20.0 | −0.98 | 10.5 | −0.34 | 3.60 | 0.36 | 6.8 |
| 2.00 | −1.10 | 22.2 | 0.22 | 12.1 | 0.28 | 3.20 | −0.17 | 9.3 |
| TOTAL | 3.08 | | 0.77 | | −0.51 | | −2.09 | |

Z-COMPONENT

| Ht($km$) | $\langle$HAD$\rangle$ | HAD$_\sigma$ | $\langle$VAD$\rangle$ | VAD$_\sigma$ | $\langle$DIV$\rangle$ | DIV$_\sigma$ | $\langle$TILT$\rangle$ | TILT$_\sigma$ |
|---|---|---|---|---|---|---|---|---|
| 0.25 | −0.51 | 7.6 | 0.26 | 5.4 | −0.21 | 1.44 | 0.10 | 6.1 |
| 0.50 | −0.40 | 9.4 | 0.73 | 5.8 | −0.07 | 1.00 | −0.61 | 6.9 |
| 0.75 | −0.42 | 8.1 | 1.00 | 8.4 | 0.09 | 0.95 | −0.86 | 9.8 |
| 1.00 | −0.13 | 9.7 | 0.37 | 7.3 | 0.19 | 1.30 | −0.79 | 8.0 |
| 1.50 | −1.40 | 12.7 | 0.12 | 8.8 | 0.04 | 1.40 | −0.22 | 8.2 |
| 2.00 | −1.70 | 13.3 | 1.20 | 7.7 | 0.05 | 0.80 | −0.56 | 8.8 |
| TOTAL | −4.56 | | 3.68 | | −0.09 | | −2.94 | |

the standard deviations may be considered their typical values. Inspection of Table 8 reveals that HAD is the largest of all the terms for $\xi$ and $\eta$ budgets with VAD and TILT being the next higher terms, respectively. Term DIV is the smallest of all terms for all three components. TILT dominates the VAD term in the $\zeta$ budget and has the strongest typical value of all term within the $\zeta$ budget at 0.75 *km*. It was shown earlier that the $\xi$-component of vorticity was the strongest component and, therefore, its budget has the strongest terms of all three directions.

The last row in Table 8 represents the vertical total of the area means for $\xi$ with HAD, VAD and TILT being nearly equal. HAD and TILT play opposite roles as source and sink for $\eta$ as do VAD and DIV but to a lesser degree. It appears that the advection terms are nearly balanced by the divergence and tilting terms for this direction. The final budget, $\zeta$, indicates that VAD is the source, while the other terms are all acting to decrease positive $\zeta$.

Table 9 lists the area means and standard deviations for the microburst domain budget terms. As expected, the typical magnitudes (standard deviations) are larger in the microburst domain as compared to those in the storm domain for each term at virtually every level. The hierarchy of significance remains as in the storm domain as HAD, VAD, TILT and DIV for the $\xi$ and $\eta$ budgets. The $\zeta$ budget again has VAD and TILT being very close in magnitude.

The vertically totaled area means are found in the last row of Table 9. Note that HAD acts to decrease (sink) $\xi$, while the remaining terms provide a source of positive $\xi$. VAD and TILT have the largest totals, but the deficit attributed to HAD cuts the source due to VAD in half. The positive contributions from DIV and TILT are roughly five and six times, respectively, those at the storm domain. This points out the significance of the microburst flow field towards the generation of $\xi$. The $\eta$ budget, on the other hand, shows (via the vertical total row) the same trend as at the storm domain. That is, HAD and VAD are sources of $\eta$, while DIV and TILT are sinks. The largest change occurs with VAD and DIV between domains. VAD develops to become the dominant source term and DIV increases fourfold to virtually match TILT as a sink. Yet again, the sources remain due to HAD and VAD. For the $\zeta$-component, VAD and TILT dominate the budget terms with VAD the source and TILT the sink. The decrease in HAD seems to indicate that the horizontal gradients of $\zeta$ are weaker on average than the vertical gradients. Furthermore, as VAD is acting to bring positive $\zeta$ values lower into the storm, TILT appears to singlehandedly spin down the positive values. Note that terms VAD and TILT have the same order of magnitude, but opposite sign throughout the whole boundary layer.

Table 9. Same as Table 8 except for the microburst domain (5 *km* × 5 *km*).

X-COMPONENT

| Ht(*km*) | ⟨HAD⟩ | $HAD_\sigma$ | ⟨VAD⟩ | $VAD_\sigma$ | ⟨DIV⟩ | $DIV_\sigma$ | ⟨TILT⟩ | $TILT_\sigma$ |
|---|---|---|---|---|---|---|---|---|
| 0.25 | 3.80 | 35.9 | −3.10 | 16.4 | 0.45 | 4.9 | 1.90 | 13.9 |
| 0.50 | −0.20 | 28.9 | −6.60 | 28.2 | −0.57 | 4.4 | 1.60 | 15.9 |
| 0.75 | −4.80 | 27.3 | 1.00 | 18.6 | −0.25 | 3.3 | 1.40 | 11.0 |
| 1.00 | −1.40 | 20.3 | 8.30 | 24.5 | 1.30 | 3.7 | 2.90 | 8.7 |
| 1.50 | 0.48 | 25.5 | 3.60 | 19.1 | 0.84 | 4.6 | 0.49 | 10.7 |
| 2.00 | −1.10 | 32.5 | 3.40 | 12.9 | 0.32 | 4.8 | −0.42 | 15.2 |
| TOTAL | −3.22 | | 6.60 | | 2.09 | | 7.87 | |

Y-COMPONENT

| Ht(*km*) | ⟨HAD⟩ | $HAD_\sigma$ | ⟨VAD⟩ | $VAD_\sigma$ | ⟨DIV⟩ | $DIV_\sigma$ | ⟨TILT⟩ | $TILT_\sigma$ |
|---|---|---|---|---|---|---|---|---|
| 0.25 | −0.55 | 23.6 | 2.40 | 13.2 | 0.36 | 3.8 | −1.20 | 12.2 |
| 0.50 | 0.64 | 33.6 | 5.70 | 24.2 | −0.18 | 3.0 | −0.17 | 17.4 |
| 0.75 | 1.90 | 39.7 | 3.90 | 18.6 | −0.09 | 3.2 | −0.43 | 17.1 |
| 1.00 | 2.90 | 26.6 | −4.40 | 20.4 | −1.60 | 3.7 | 0.32 | 10.7 |
| 1.50 | 1.60 | 23.8 | −2.60 | 14.2 | −0.89 | 4.8 | −0.00 | 9.2 |
| 2.00 | −1.40 | 28.2 | 1.80 | 17.1 | 0.38 | 4.6 | −0.72 | 13.1 |
| TOTAL | 5.09 | | 6.80 | | −2.02 | | −2.21 | |

Z-COMPONENT

| Ht(*km*) | ⟨HAD⟩ | $HAD_\sigma$ | ⟨VAD⟩ | $VAD_\sigma$ | ⟨DIV⟩ | $DIV_\sigma$ | ⟨TILT⟩ | $TILT_\sigma$ |
|---|---|---|---|---|---|---|---|---|
| 0.25 | 0.43 | 11.6 | 0.37 | 8.7 | 0.03 | 1.3 | 0.63 | 9.2 |
| 0.50 | 1.30 | 13.4 | 0.93 | 9.0 | −0.22 | 1.2 | −1.30 | 8.1 |
| 0.75 | 0.39 | 7.8 | 1.50 | 12.9 | 0.12 | 1.0 | −2.50 | 13.0 |
| 1.00 | −0.14 | 10.7 | 3.50 | 9.9 | 0.18 | 1.4 | −3.90 | 9.4 |
| 1.50 | −0.46 | 10.9 | 3.60 | 12.9 | 0.11 | 1.7 | −3.50 | 9.8 |
| 2.00 | −2.20 | 15.7 | 1.70 | 10.9 | 0.53 | 2.3 | −0.66 | 11.7 |
| TOTAL | −0.68 | | 11.60 | | 0.75 | | −11.23 | |

## 5. CONCLUSIONS

Budgets for each vorticity component were assessed at every analysis level from the Doppler derived winds and their derivatives. In addition, spatial variations of three vorticity components were computed throughout the boundary layer.

Results show that horizontal vorticity centers were found in regions of strong horizontal gradients of vertical velocity and in areas with large vertical shear of the horizontal winds. The simple case had a nearly circular-symmetric microburst with a vortex ring surrounding the microburst down flow. This ring descended from 0.75 *km* at 1647 MDT to 0.5 *km* at 1649 MDT. The effect was to create increased surface winds southwest and northeast along the gust fronts as the ring descended. The complex case showed the evolution of a misocyclone. A positive value of vertical vorticity was generated from top down similar to that reported in Kessinger *et al.* (1988).

Vorticity budget analyses reveal the magnitude of each term in the budget

equation to be greater in the microburst domain than in the storm domain. This indicates that the strongest forcing and advection occurred within small regions of the storms. The existence of the microburst enhanced the magnitude of the vorticity components in the near microburst region of the storm. This was true for both cases and for each component of vorticity.

The differences in storm structure allow examination of the vorticity of a microburst embedded within a relatively simple flow field and that of a microburst within a complicated flow field. This resulted in different vorticity distributions and budgets.

Further study is needed to determine why the rotors develop in some cases are not in others. With sufficient time resolution, the propagation of these vortices and rotors may be studied. The solenoidal term, although believed to be small, may contribute in the head of the gust front. This may be important in the formation of the rotor.

*Acknowledgements.* The authors wish to thank the National Center for Atmospheric Research (NCAR) for providing the dual-Doppler data and technical assistance. We are grateful to Robert Pasken and John Coover for their help in data analysis and reduction. Thanks also go to William McNamee for his assistance in computation. This research was partially supported by the Division of Atmospheric Sciences, National Science Foundation, under Grant ATM-8312172. P. G. Lapointe was supported by the Air Force Institute of Technology.

## REFERENCES

Droegemeier, K. K., and R. B. Wilhemson, 1985: Three-dimensional numerical modeling of convection produced by interacting thunderstorm outflows. Part I: Control simulation and low-level moisture variations, *J. Atmos. Sci.*, **42**, 2381–2403.

Fujita, T. T., 1985: The Downburst Microburst and Macroburst, University of Chicago Press, Chicago, 122 pp.

Kessinger, C. J., D. B. Parsons, and J. W. Wilson, 1988: Observations of a storm containing misocyclones, downbursts, and horizontal vortex circulations. *Mon. Weather Rev.*, **116**, 1959–1982.

Lin, Y. J., and R. G. Hughes, 1987: Structural features of a microburst-producing storm in Colorado revealed by JAWS dula-Doppler radars, *J. Atmos, Sci.*, **44**, 3640–3655.

Lin, Y. J., W. E. McNamee, and J. A. Coover, 1991: Observational study of a multiple microburst-producing storm. Part I: Kinematic, dynamic, and thermodynamic structures, TAO, **2**, 95–119.

Lin, Y. J., and J. A. Coover, 1991: Observational study of a multiple microburst- procucing storm. Part II: A comparison between the simple case and the comples case, TAO, **2**, 121–145.

Linden, P. F., and J. E. Simpson, 1985: Microburst: A hazard for aircraft, Nature, **317**, 601–602.

Parsons, D. B., C. J. Kessinger, K. L. Elmore, and R. D. Roverts, 1985: An investigation into the forcing of microbursts, Prepints, 14th Conference on Severe Local Storms, Indianapolis, *Amer. Meteor. Soc.*, 48–51.

Waranauskas, B. R., 1985: The rotor microburst: A new explanation for burst swath damage, Preprints, 14th Conference on Severe Local Storms, Indianapolis, *Amer. Meteor. Soc.*, 260–263.

# 產生微爆雷雨系統之觀測研究（三）渦度收支

林永哲 P. G. Lapointe
美國聖路易大學 地球與大氣科學系
美國空軍氣象勤務中心

## 摘要

本文分析了兩個產生微爆（microburst）雷雨系統之雙都普勒風場，並以此風場計算三維渦度收支。在這兩個科羅拉多州的個案中，一個發生於 1982年7月14日，是屬於單次微爆類。另一個發生於 1982年8月5日，是屬於多次微爆類。

結果顯示：水平渦度的中心，垂直速度水平梯度最大區，和最大垂直風切區，皆位於同一位置。這些最大梯度區沿著下衝外流空氣所形成之陣風鋒面分佈，在低層風速最大的區域上方，有一水平渦度中心。

從渦度收支可看出：平流、幅散、傾斜等項的貢獻，在微爆發生的區域，比在暴風雨系統中其他區域大。這表示環境對系統動力之影響及平流都主要發生在很小的範圍內。本次兩個案中，微爆的輻散外流，會減弱微爆區域中存在的任何正值渦度。

兩個個案渦度分佈的比較，有助於瞭解單一近似圓形之微爆與複雜氣流之多次微爆之間的差異。